

See discussions, stats, and author profiles for this publication at: <https://www.researchgate.net/publication/231170354>

Extension of sedimentation/steric field-flow fractionation into submicron range: Size analysis of 0.2–15 μm metal particles

ARTICLE *in* ANALYTICAL CHEMISTRY · DECEMBER 1992

Impact Factor: 5.64 · DOI: 10.1021/ac00047a027

CITATIONS

25

READS

18

2 AUTHORS, INCLUDING:



Myeong Hee Moon

Yonsei University

150 PUBLICATIONS 2,416 CITATIONS

SEE PROFILE

Extension of Sedimentation/Steric Field-Flow Fractionation into the Submicrometer Range: Size Analysis of 0.2–15- μm Metal Particles

Myeong Hee Moon and J. Calvin Giddings*

Field-Flow Fractionation Research Center, Department of Chemistry, University of Utah, Salt Lake City, Utah 84112

Sedimentation/steric field-flow fractionation (FFF), a rapid method for the high-resolution separation and characterization of $>1\text{-}\mu\text{m}$ -diameter particles, can be extended well into the submicrometer size range providing the steric inversion (or transition) diameter d_i , normally about $1\text{ }\mu\text{m}$, is significantly lowered. To better accomplish this, a means has been developed to predict d_i based on normal mode retention theory and steric mode calibration plots. By applying a high field strength, d_i can be systematically reduced below $1\text{ }\mu\text{m}$ and steric FFF analysis extended down to the modified d_i value. To offset the increased elution time associated with the smaller d_i , channel thickness and breadth are reduced and high channel flow rates utilized. The high flow rates and slow flow (rather than stop-flow) injection reduce sample losses at the channel wall. The above concepts were verified using polystyrene latex standards. Application was made to samples of gold, palladium, silver, and copper particles. A single steric calibration plot, obtained by electron microscopy for gold particles, was applied to the size analysis of various metals using the density compensation method. For these runs $d_i \sim 0.2\text{ }\mu\text{m}$. (Much smaller sizes than d_i can be analyzed by normal mode FFF but then larger sizes are excluded.) Analysis times ranged from 1 to 12 min depending on the smallest particle size.

INTRODUCTION

Sedimentation field-flow fractionation (SdFFF) has become an effective tool for the size (and in some cases the density) characterization of particulate samples. High-resolution particle size analysis in the submicrometer size range has been demonstrated repeatedly using the normal mode of sedimentation FFF.^{1–8} More recently, techniques have been developed for the calibration and size analysis of supramicrometer ($>1\text{ }\mu\text{m}$) sized particles using the steric mode of sedimentation FFF, or Sd/StFFF.^{9–11} Analysis in the steric mode has provided even higher resolution than that typical

for the normal mode and the analysis is often 1 order of magnitude faster. Thus there is a significant motivation for expanding the size range of steric mode operation, extending this range if possible to submicrometer diameters. This downward extension would also help solve the steric inversion problem that arises in attempts to analyze samples having both submicrometer and supramicrometer sized particles.¹²

An extension downward of the applicable size range of Sd/StFFF requires that the steric inversion diameter d_i (the transition diameter between steric and normal mode operation) be lowered because steric FFF cannot be applied to particles with diameters smaller than d_i . Thus part of this work is devoted to a study of factors affecting d_i . While previous studies have examined the influence of various parameters (especially the field strength) that influence d_i in sedimentation FFF,^{12,13} it has been difficult to make accurate predictions because it has not been possible to fully characterize the steric correction factor γ , which has an important influence on d_i . In this paper we show that it is possible to formulate γ in terms of the calibration constants applicable to Sd/StFFF size analysis.

A parallel need exists in flow FFF to drive the inversion diameter to lower values as has been noted in recent studies.¹⁴ The procedure developed here for estimating d_i under different experimental conditions should be transferable to flow FFF. In either case it is best to work with relatively thin channels, high field strengths, and high flow velocities as explained below.

In the normal mode of FFF (either sedimentation FFF or flow FFF) retention time increases with particle diameter d until d reaches d_i , which is the upper limit of normal mode operation¹² (see Figure 1). Conversely, in the steric mode, applicable to larger particles, the retention time increases as d decreases until $d = d_i$, the minimum diameter to which steric FFF is applicable. Thus particles whose diameters are close to d_i are retained for longer times than particles of any other diameter, as made clear by Figure 1. Furthermore, as d_i is made smaller by the adjustment of parameters, the retention time is driven to still higher levels and can exceed the void time of the channel by over 2 orders of magnitude. Therefore as d_i is driven to lower levels to expand the range of applicability of steric FFF, retention times inevitably become excessive. In addition, sample dilution and subsequent detectability becomes an increasingly serious concern. However, at a given volumetric flow rate the retention time can be greatly reduced and sample dilution countered by using

* Corresponding author.

(1) Yang, F. J.; Myers, M. N.; Giddings, J. C. *J. Colloid Interface Sci.* 1977, 60, 574–577.

(2) Yang, F.-S.; Caldwell, K. D.; Giddings, J. C. *J. Colloid Interface Sci.* 1983, 92, 81–91.

(3) Kirkland, J. J.; Dilks, C. H., Jr.; Yau, W. W. *J. Chromatogr.* 1983, 255, 255–271.

(4) Beckett, R. *Environ. Tech. Lett.* 1987, 8, 339–354.

(5) Oppenheimer, L. E.; Smith, G. A. *J. Chromatogr.* 1989, 461, 103–110.

(6) Beckett, R.; Hotchin, D. M.; Hart, B. T. *J. Chromatogr.* 1990, 517, 435–447.

(7) Li, J.; Caldwell, K. D.; Mächtle, W. *J. Chromatogr.* 1990, 517, 361–376.

(8) Giddings, J. C.; Myers, M. N.; Moon, M. H.; Barman, B. N. In *Particle Size Distribution II: Assessment and Characterization*; ACS Symposium Series 472; Provder, T., Ed.; American Chemical Society: Washington, DC, 1991; pp 198–216.

(9) Giddings, J. C.; Moon, M. H.; Williams, P. S.; Myers, M. N. *Anal. Chem.* 1991, 63, 1366–1372.

(10) Williams, P. S.; Moon, M. H.; Giddings, J. C. In *Proceedings of 25th Anniversary Conference on Particle Size Analysis (PSA 91)*; Stanley-Wood, N., Lines, R., Eds.; Royal Society of Chemistry: Cambridge, UK, in press.

(11) Giddings, J. C.; Moon, M. H. *Anal. Chem.* 1991, 63, 2869–2877.

(12) Lee, S.; Giddings, J. C. *Anal. Chem.* 1988, 60, 2328–2333.

(13) Myers, M. N.; Giddings, J. C. *Anal. Chem.* 1982, 54, 2284–2289.

(14) Ratanathanawongs, S. K.; Giddings, J. C. In *Size Exclusion Chromatography and Field-Flow Fractionation*; ACS Symp. Series; Provder, T., Ed.; American Chemical Society: Washington, D.C., in press.

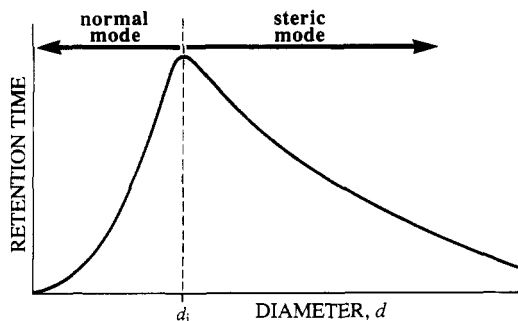


Figure 1. Plot showing way in which retention time depends upon particle diameter above and below the steric inversion diameter d_i .

a thinner channel (see below). The retention time can be further reduced by decreasing the breadth (the edge-to-edge distance) of the channel.

Particles having diameters close to d_i (and thus considered to be in the steric transition region) are strongly influenced by both normal and steric mechanisms of retention. In order to characterize retention in the steric transition region, it is necessary to have quantitative descriptions of (1) retention in the normal mode, (2) retention in the steric mode, and (3) the way in which normal and steric mode retention act jointly in the transition region. Insofar as category 1 is concerned, normal mode retention can be well described by basic FFF theory.¹⁵ With regard to category 3, it has been established that the retention ratio R can be approximated (providing R is small) as the sum of the retention ratios originating when the normal and steric mechanisms are acting alone.¹² Thus the biggest uncertainty lies in category 2 in which the description of steric mode retention has been complicated by hydrodynamic lift forces and their influence on the steric correction factor γ .¹⁶ However, in recent work we have developed a calibration procedure to better characterize retention in sedimentation/steric FFF.⁹

The steric calibration procedure is based on the measurement of the retention times of a series of polystyrene latex standards, a process that takes only a few minutes. Since sedimentation forces depend upon the density difference $\Delta\rho$ between the particle and the carrier solution, a density compensation procedure is invoked in which the field strength G for the sample of interest is adjusted in such a way that the product $G\Delta\rho$ is the same for the sample as for the latex standards. For this fixed $G\Delta\rho$ value, a plot of the logarithm of retention time versus the logarithm of d produces a straight-line calibration plot.⁹ The plot is applicable to particles of different composition and density as long as $G\Delta\rho$ is held constant. This plot persists until diameters become so small (approaching d_i) that retention is substantially perturbed by the normal mode mechanism.

In this paper we have combined the three essential elements of retention described above to express mathematically the retention behavior of particles over a very broad range of diameters. This range extends from the submicrometer extremes of the normal mode to the supramicrometer diameters subject to steric mode analysis. The theoretical expressions are tested using polystyrene latex microspheres and found to be in good agreement with experimental measurements.

Both present and previous theoretical analyses have shown that d_i can be reduced by an increase in the product $G\Delta\rho$.^{12,13} We show here that by using relatively high G values (894 gravities), the d_i of polystyrene latex beads can be reduced

to 0.60 μm . However, the $\Delta\rho$ of polystyrene in dilute aqueous solutions is so low (0.05 g/cm³) that $G\Delta\rho$ could be pushed no higher than $4.4 \times 10^4 \text{ g/cm}^2\text{s}^2$. Fortunately, metal particles, for which $\Delta\rho$ is several hundred times higher, are not subject to this limitation, and $G\Delta\rho$ can be sufficiently increased (up to $3.8 \times 10^6 \text{ g/cm}^2\text{s}^2$) to drive d_i down to 0.21 μm .

The high $G\Delta\rho$ values needed for submicrometer steric FFF analysis give rise to concerns that particles will be driven so forcefully to the channel accumulation wall that they will adhere to the wall and thus fail to elute. Such particle-wall adhesion can be offset by high shear rates which in our case are generated by high flow velocities and thin channels. However, in the usual procedure of stop-flow injection, flow is temporarily halted after sample introduction to allow relaxation to occur under the influence of the applied field. This stop-flow period, unfortunately, affords an ideal opportunity for particle-wall adhesion to occur providing that a tendency toward adhesion exists. Such adhesion may or may not be reversed once flow resumes. This window of opportunity for adhesion can be largely closed by continuing flow during relaxation. The flow rate applied in this period is chosen by compromise: high flow rates enhance relaxational band broadening and lower flow rates make adhesion more likely. The compromise flow rate is often lower than the flow rate used for the run, leading to the expression *slow flow injection procedure*.¹⁷ This procedure was utilized here.

Our work on metal particles at high values of $G\Delta\rho$ poses a calibration problem. Since the $G\Delta\rho$ levels applied to metals could not be reached using polystyrene latex calibration standards, another calibration procedure had to be devised. The new calibration procedure involves the use of a single metal (gold) sample which was run in the system and fractions collected at short time intervals. The mean particle diameter in each fraction was measured microscopically, and this value, combined with the time recorded for its collection, was used to construct a calibration plot expressing (in logarithmic form) the dependence of retention time on particle diameter. This same calibration plot could then be used for other metal particles using the density compensation principle, $G\Delta\rho = \text{constant}$.

It was noted above that steric FFF retention times increase significantly as one goes to smaller particle diameters but that this increase could be offset by using a thinner channel of lower volume. The rationale for changing channel dimensions to offset excessive times is given below.

For a given retention ratio R (the ratio of the downstream displacement velocity of the particles to the mean carrier fluid velocity) and volumetric flow rate \dot{V} , the retention time of a sample is proportional to the channel void time t^0 . Reducing the channel thickness from the usual 254 to 127 μm and the breadth from the usual 2 to 1 cm creates a channel with a void volume of just over 1 mL as compared to the usual 4–5 mL. The reduced channel volume provides a fourfold reduction in t^0 and thus in retention time at constant \dot{V} . Furthermore, because R is inversely proportional to channel thickness, another factor of 2 becomes available. The 8-fold retention time reduction can be used to speed elution directly and/or to ease the requirement of a high volumetric flow rate. In addition, with the 2-fold reduction in channel thickness, sample detectability improves approximately 4-fold. These features are largely responsible for making feasible the application of steric FFF to smaller particles.

THEORY

The retention ratio R for particles of diameter d in sedimentation FFF can be written quite generally as the sum

(15) Giddings, J. C.; Yang, F. J. F.; Myers, M. N. *Anal. Chem.* 1974, 46, 1917–1924.

(16) Williams, P. S.; Koch, T.; Giddings, J. C. *Chem. Eng. Commun.* 1992, 111, 121–147.

(17) Moon, M. H.; Myers, M. N.; Giddings, J. C. *J. Chromatogr.* 1990, 517, 423–433.

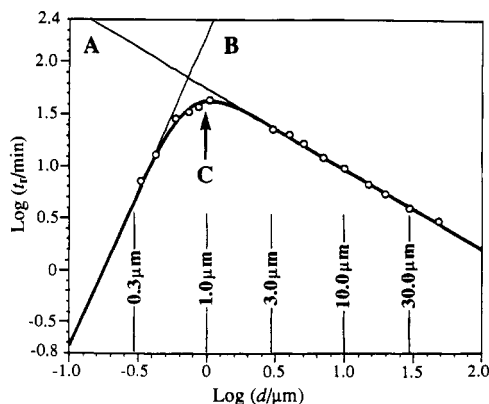


Figure 2. Logarithmic calibration plot of retention time t_r versus particle diameter d for 14 polystyrene latex standards ranging in diameter from 0.330 to 47.9 μm . All data were obtained in channel I at 800 rpm and $V = 7.0$ mL/min. Plots A, B, and C represent retention in the steric, normal, and transition regions, respectively.

of two terms¹²

$$R = \frac{t^0}{t_r} = \frac{36kT}{\pi d^3 G \Delta \rho w} + \frac{3\gamma d}{w} \quad (1)$$

where t^0 is the void time (the passage time of a nonretained material), t_r is the retention time, kT is the thermal energy, w is channel thickness, G is acceleration, $\Delta \rho$ is the density increment, and γ is a steric correction factor. The first term on the right-hand side (rhs) of eq 1 represents the retention ratio for the normal mode of FFF and the last term is the retention ratio for the steric mode of FFF. Earlier work¹⁸ suggested a simple approximation for the steric correction factor γ as

$$\gamma = C' \langle v \rangle^\alpha d^{-\beta} \quad (2)$$

where C' is a constant, $\langle v \rangle$ is the mean flow velocity in the channel, and the exponents α and β are constants to be determined empirically. At a given flow rate, eq 2 can be simplified to

$$\gamma = C d^{-\beta} \quad (3)$$

Constants C and β can be obtained from the parameters of a steric calibration plot. As noted in the initial development of the calibration procedure,⁹ a plot of $\log t_r$ versus $\log d$ for steric FFF normally yields a straight calibration line (as illustrated by line A in Figure 2) expressed as

$$\log t_r = -S_d \log d + \log t_{r1} \quad (4)$$

where $-S_d$, the negative slope of the plot, is the diameter based selectivity and t_{r1} is a constant equal to the extrapolated value of t_r for particles of unit diameter. Values of S_d and t_{r1} are generally obtained from a single calibration run using polystyrene latex standards.⁹

Considering the retention ratio of the steric mode only, we can substitute eq 3 into the last part of eq 1 and thus obtain the steric mode t_r

$$t_r = \frac{t^0 w}{3\gamma d} = \frac{t^0 w}{3C d^{1-\beta}} \quad (5)$$

The logarithmic expression of eq 5 is

$$\log t_r = -(1-\beta) \log d + \log \frac{t^0 w}{3C} \quad (6)$$

Equation 6 is identical in form to eq 4. Thus the required constants C and β can be obtained in terms of the measured calibration constants S_d and t_{r1} by equating these two expressions, which yields

$$\beta = 1 - S_d \quad (7)$$

$$C = \frac{t^0 w}{3t_{r1}} \quad (8)$$

The substitution of eqs 3 (or 2), 7, and 8 into eq 1 thus yields a general expression for R and t_r in terms of d and a set of known or measurable parameters

$$R = \frac{t^0}{t_r} = \frac{36kT}{\pi d^3 G \Delta \rho w} + \frac{t^0 d^{S_d}}{t_{r1}} \quad (9)$$

The steric inversion of transition diameter d_i is defined as the d for which $\partial R / \partial d = 0$. Particles of this diameter have maximum retention or minimum R . Differentiation of eq 9 gives

$$\frac{\partial R}{\partial d} = \frac{-108kT}{\pi d^4 G \Delta \rho w} + \frac{t^0}{t_{r1}} S_d d^{S_d-1} \quad (10)$$

Thus

$$d_i = \left\{ \frac{108kT t_{r1}}{\pi G \Delta \rho w t^0 S_d} \right\}^{1/(S_d+3)} \quad (11)$$

which gives d_i in terms of known parameters, particularly in terms of $G \Delta \rho$ which can be varied widely by changes in field strength G .

The dependence of d_i on $G \Delta \rho$ shown by eq 11 is somewhat misleading because t_{r1} increases with $G \Delta \rho$ raised to a power of approximately 0.2.¹¹ With $S_d \approx 0.75$, d_i is seen to depend on $G \Delta \rho$ raised to the approximate power -0.213 . The relative insensitivity of d_i to $G \Delta \rho$ means that large changes in $G \Delta \rho$ must be realized to gain small changes in d_i . (Thus a 26-fold increase in $G \Delta \rho$ is needed to achieve a 2-fold reduction in d_i .) Fortunately, G can be varied over wide limits, and the modest changes induced in d_i can be quite useful. However, as noted earlier, high $G \Delta \rho$ values increase the risk of depositing particles at the wall and thus losing them. This risk can be offset by using various hydrodynamic¹⁹ or dynamic (as opposed to stop-flow) injection techniques including slow flow injection¹⁷ as utilized here. Sample loss can also be reduced by using higher flow rates which, as shown below, may have the small secondary benefit of leading to further reductions in inversion diameter d_i .

With the constant term C replaced by $C' \langle v \rangle^\alpha$ in order to account for flow velocity changes, eq 11 is replaced by

$$d_i = \left\{ \frac{36kT}{C' \pi S_d G \Delta \rho \langle v \rangle^\alpha} \right\}^{1/(S_d+3)} \quad (12)$$

where α is to be determined by comparing calibration plots obtained at different flow rates. Based on previous experimental work,^{11,18} values of α appear to lie in the range from 0.1 to 0.3. Equation 12 shows that the steric inversion diameter decreases with the mean flow velocity $\langle v \rangle$ raised to the $\alpha/(S_d+3)$ power, equal only to 0.03–0.08. (Another power of ~ 0.05 may arise because S_d appears to increase with $\langle v \rangle$ —see Table II.) Thus if the overall power is ~ 0.1 , a 10-fold change in $\langle v \rangle$ yields $\sim 20\%$ decrease in d_i . This conclusion is rather tentative because of the uncertainties in the above dependencies. However, high $\langle v \rangle$ values (more specifically, high shear rates) are still essential for high speed and for preventing particle-wall adhesion whether or not they substantially lower d_i .

The full retention curve (including the steric transition) written in a logarithmic form that can be compared to the

(18) Peterson, R. E., II; Myers, M. N.; Giddings, J. C. *Sep. Sci. Technol.* 1984, 19, 307–319.

(19) Liu, M.-K.; Williams, P. S.; Myers, M. N.; Giddings, J. C. *Anal. Chem.* 1991, 63, 2115–2122.

steric-mode retention expression of eq 4 is obtained from eq 9

$$\log t_r = \log t^0 - \log \left[\frac{36kT}{\pi d^3 G \Delta \rho w} + \frac{t^0}{t_{r1}} d^{S_d} \right] \quad (13)$$

The particle size distribution $m(d)$ for a broadly distributed particle sample retained by Sd/StFFF can be expressed as⁹

$$m(d) = \frac{c(t_r) \dot{V} S_d t_{r1}}{d^{S_d+1}} = c(t_r) \dot{V} S_d t_{r1} \left[\frac{t_r}{t_{r1}} \right]^{(S_d+1)/S_d} \quad (14)$$

where $c(t_r)$ is the concentration of eluting particles versus retention time, a function obtained from the experimental fractogram. (The true concentration is obtained by applying a light scattering correction to the measured detector signal.) Quantity \dot{V} is the volumetric flow rate. Equation 14 can be used to obtain the particle size distribution from the fractogram provided the calibration constants S_d and t_{r1} are known from a calibration curve.

Equation 14 is applicable to the linear portion of the plot in Figure 2, specifically to line A which is described by eq 4. The calibration can be extended on down to a point very close to the steric inversion diameter (thus allowing for some of the curvature in Figure 2 developing near the maximum in t_r) by using the somewhat more general expression⁹

$$m(d) = c(t_r) \dot{V} \left| \frac{dt_r}{dd} \right| \quad (15)$$

where the derivative function dt_r/dd can be obtained from eq 9.

If the calibration equations valid for (but limited to) Sd/StFFF are applied to particles in the steric transition region with sizes only slightly larger than d_i , two discrepancies will arise. First the retention time t_r will be somewhat smaller than predicted, and thus the size calculated on the basis of the observed t_r will be too large. Second, the size distribution function $m(d)$ will be too large for these diameters because the diminishing slope $|dt_r/dd|$ in eq 15 found as $d \rightarrow d_i$ is not reflected in eq 14. (These two errors will partially offset one another when the size distribution tails off just above d_i .)

The magnitude of the errors incurred can be most generally formulated by expressing retention in terms of the dimensionless particle diameter

$$\Delta = d/d_i \quad (16)$$

When this is done using eq 11 for d_i , eq 9 becomes

$$R = K \left(\frac{1}{\Delta^3} + \frac{3}{S_d} \Delta^{S_d} \right) \quad (17)$$

where constant K is

$$K = \left(\frac{36kT}{\pi G \Delta \rho w} \right)^{S_d/(S_d+3)} \left(\frac{t^0 S_d}{3t_{r1}} \right)^{3/(S_d+3)} \quad (18)$$

Based on eq 17, the ratio of the actual t_r to the t_r predicted on the basis of steric mode retention acting alone (in which case the $1/\Delta^3$ term is neglected) is given by

$$r_t = \frac{t_r(\text{actual})}{t_r(\text{steric})} = \frac{1}{1 + (S_d/3)\Delta^{-(S_d+3)}} \quad (19)$$

A plot of eq 19 is shown in Figure 3. It is seen that even at the steric inversion diameter ($\Delta = 1$), the actual t_r drops only to about 80% of the value predicted from the steric calibration equations; at $d = 1.5d_i$ ($\Delta = 1.5$), t_r is 95% of the sterically predicted t_r .

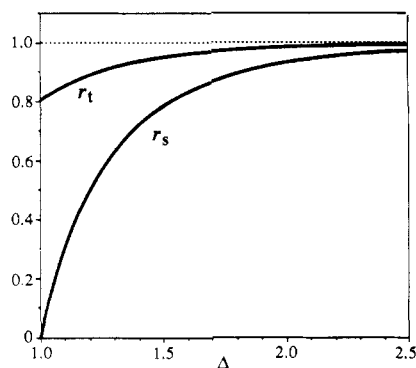


Figure 3. Plots showing errors incurred (as measured by the departure of the r_t and r_s lines from unity) in retention time t_r and in slope dt_r/dd when using uncorrected steric calibration plot in the steric transition region.

The slope (or derivative) term in eq 15 can be obtained from

$$\frac{dt_r}{dd} = \frac{dt_r}{dR} \frac{dR}{d\Delta} \frac{d\Delta}{dd} \quad (20)$$

Using eqs 1, 16, and 17, this becomes

$$\frac{dt_r}{dd} = \frac{3Kt^0}{d_i R^2} \left(\frac{1}{\Delta^4} - \Delta^{S_d-1} \right) \quad (21)$$

which, of course, is zero at $\Delta = 1$. The ratio of slopes for Δ values near unity is approximated by

$$r_s = \frac{(dt_r/dd)(\text{actual})}{(dt_r/dd)(\text{steric})} \approx 1 - \Delta^{-(S_d+3)} \quad (22)$$

which applies for any fixed value of t_r and thus R in the steric transition region. This ratio is also plotted in Figure 3. The plot shows that the slope reaches ~50% of the steric value at $\Delta = 1.2$ and ~90% at $\Delta = 1.9$. Thus eq 14 (based on the steric slope) is quite accurate for $\Delta \geq 2$ and reasonably accurate ($r_s \geq 0.78$) for $\Delta \geq 1.5$.

While eq 14 has been used to obtain particle size distributions in this work, leading to some error for smaller d values near d_i as described above, nothing precludes the use of eq 15 for this purpose to enhance the accuracy for particles close to the inversion diameter.

EXPERIMENTAL SECTION

The sedimentation FFF system used in this study is in most respects identical to the model S101 Colloid/Particle Fractionator from FFFractionation, Inc. (Salt Lake City, UT). Two different channels were utilized. Channel I has rather conventional dimensions with a breadth b of 1.7 cm, a thickness w of 254 μm , and a tip-to-tip length L_{tt} of 90 cm. Channel II has reduced dimensions: $b = 1$ cm, $w = 127 \mu\text{m}$, and $L_{tt} = 90$ cm. The void volumes, as measured by the nonretained volume of a sodium benzoate peak (from which a dead volume of ~0.2 mL is subtracted), are 4.0 mL for channel I and 1.2 mL for channel II. The radii of rotation are 15.7 cm for I and 15.1 cm for II.

Polystyrene latex standards, used for the initial evaluation of steric transition points, have nominal diameters of 0.33, 0.426, 0.596, 0.742, 0.868, 3.983, 5.002, 7.04, 9.83, 15.0, 19.58, 29.12, and 47.9 μm . These were obtained from Duke Scientific (Palo Alto, CA). A 1.05- μm standard was obtained from Polysciences (Warrington, PA). The identities and characteristics of the several types of metal particles studied in this work are tabulated in Table I. These metal particles were provided by Mr. Dan V. Goia of Metz Metallurgical Corp. (South Plainfield, NJ).

An FMI Lab Pump Model QD-2 (Fluid Metering, Inc., Oysterbay, NY) was used for high channel flow rates. Another pump, a Kontron HPLC Pump Model 410 (Kontron Electrolab, London, UK) was used for sample injection during the slow flow injection procedure employed for the separation of metal particles.

Table I. Identification and Characteristics of Metal Particles Provided by Metz Metallurgical Corp.^a

sample ID and batch no.	density (g/cm ³)	diameters at cumulative mass point (μm)					
		L & N ^b			FFF		
		90%	50%	10%	90%	50%	10%
a. gold 2000 (7-51755-0)	19.2	5.02	2.60	1.28	2.15	1.63	1.19
b. gold 1900 (7-23363-0)	19.2	0.98	0.59	0.35	0.86	0.48	0.36
c. palladium 3103 (7-22111-0)	11.6	0.94	0.54	0.32	0.72	0.40	0.34
d. palladium 3102 (7-22204-0)	11.6	1.01	0.58	0.35	0.57	0.34	0.30
e. silver (7-51812-0)	10.5	1.67	0.83	0.41	1.50	0.95	0.59
f. copper 50 (7-10178-0)	8.9	1.16	0.62	0.34	0.65	0.49	0.41
g. copper 10 (7-29108-0)	8.9	14.92	8.00	4.86	10.70	7.47	5.17
h. silver-palladium 3030 (7-23226-0)	11.5	2.19	1.04	0.34	1.39	0.87	0.57

^a The second set of cumulative mass distribution parameters were obtained by FFF as described in the text. ^b Sizes from Leeds & Northrup particle size analyzer as provided by Metz.

A flow rate of 5.0 mL/min, maintained for 15 s, was used for slow flow injection. Following the slow flow injection procedure, a Hamilton 3-way valve (Hamilton Co., Reno, NV) was used to convert the carrier flow from one pump to another, thus giving the high flow rate needed for separation.

The carrier liquid used for the polystyrene latex standards was doubly distilled and deionized water containing 0.1% (v/v) FL-70 (Fisher Scientific, Fair Lawn, NJ) with 0.02% (w/v) sodium azide added as a bactericide. For the characterization of metal particles, 0.07% Daxad 11-G (sodium naphthalenesulfonate-formaldehyde from W. R. Grace & Co., Lexington, MA) was used to maintain particle dispersion. The metal samples were sonicated at least 2 h to disperse the particles in the carrier liquid.

For metal sample introduction, 0.8–1.0 mg (in most cases) of metal particles was injected into the carrier stream prior to its entering the spinning FFF channel using a septum injector and a microsyringe. A slow flow injection procedure was used as described above. Latex samples, by contrast, were injected directly onto the stationary channel after which flow was halted and the channel set spinning. The stop-flow condition was maintained for a time just sufficient to allow particle relaxation across the channel thickness, following which flow was resumed to drive the particles through the channel. The eluted samples were monitored by a Spectroflow Monitor SF770 UV-vis detector (Kratos Analytical Instruments, Westwood, NJ) set at 350-nm wavelength in order to avoid UV absorption by the dispersing agent, Daxad 11-G. Fractions of eluted particles were collected by means of a Model FC-80K microfractionator from Gilson Medical Electronics (Middletown, WI). A strip chart recorder from Houston Instrument Corp. (Austin, TX) was used for recording. The recorded signal was converted to a particle size distribution based on eq 14 and implemented using computer software developed at the Field-Flow Fractionation Research Center. Each distribution was subjected to a light-scattering correction (using Mie theory for a totally reflecting sphere) in order to obtain true mass-based particle size distribution curves.

For detailed microscopic examination, a Hitachi S-450 scanning electron microscope (Hitachi Scientific Instruments, Nissei Sangyo America, Middletown, CA) was used to obtain electron micrographs of particles contained in various fractions. The collected particles were transferred onto a 13-mm Nucleopore membrane filter (Pleasanton, CA) of 0.1-μm pore size by a disposable pipet. Colloidal graphite adhesive (Ted Pella Corp., Redding, CA) was used to mount the filter on a steel stub. Particle sizes were measured (from the micrographs) with the help of a magnifier to within the nearest 0.12-μm unit. An optical microscope (Olympus Optical Co. Ltd., Tokyo) was used to examine particles in copper sample g.

RESULTS AND DISCUSSION

For the initial evaluation of retention in and beyond the steric transition region, polystyrene latex standards of sizes ranging from 0.33 to 47.9 μm were used in channel I ($w = 254$ μm). Figure 2 shows the plot of $\log t_r$ versus $\log d$ obtained for these particles at 800 rpm and $\dot{V} = 7.0$ mL/min. (A stop-flow injection method with variable stopflow times was used; these times were set equal to the calculated relaxation times,

ranging from a few seconds to ~13 min.) Plot A in Figure 2 is the empirical calibration line obtained from the larger standard particles employed for steric FFF. The nine data points used for calibration are shown on the right side of the plot. The parameters of calibration plot A (see eq 4) are 0.772 for S_d (the selectivity) and 55.6 min for $t_{r,1}$ (the extrapolated retention time of 1-μm particles) with a correlation coefficient of 0.998.

Line B of Figure 2 represents the theoretical retention time plot for particles migrating under normal-mode conditions. This plot is obtained from the first term on the rhs of eq 1. The data points for the two smallest (0.330 and 0.426 μm) particles are seen to fit the theory line fairly well. (The flow rate, $\dot{V} = 7.0$ mL/min, used in this evaluation was chosen to cover the whole range of particle sizes without excessive band broadening. Smaller particles in the submicrometer size range do broaden excessively at this high flow rate and modest field strength. Clearly these conditions are not the best for separating all particles but are a practical compromise for studying the steric transition phenomenon.) The cluster of four larger particles of diameters 0.596, 0.742, 0.868, and 1.05 clearly elute earlier than expected from normal-mode theory. These particles are substantially influenced by steric effects and thus fall in the steric transition region.

Equation 13 is used with the above calibration procedures to obtain the overall retention time curve, shown as plot C in Figure 2, that applies around and well beyond the steric transition point. This plot is specific for each set of experimental conditions (e.g., for each \dot{V} and $G\Delta\rho$ value.) The data points in Figure 2 falling in both normal and steric operating regions show good agreement with the plot. The steric inversion diameter d_i for these experimental conditions is calculated from eq 11 to be 1.02 μm. Such means for obtaining the steric inversion diameter are useful to select optimum experimental conditions to cover the desired diameter range for sedimentation FFF operating in either normal or steric modes.

Table II lists the steric transition diameters and calibration parameters acquired for various sets of experimental conditions that were employed in obtaining calibration plots for channel II ($w = 127$ μm). As the field strength and the flow rate were increased, the steric transition point for polystyrene standards was lowered, eventually to 0.6 μm for case F. Figure 4 shows the fractograms (obtained by stopless flow injection) used to acquire the calibration parameters for run conditions E and F of Table II. The ultrahigh speed separation (case F, Figure 4a) was achieved at the maximum field strength and flow rate used in this study, corresponding to 2300 rpm and $\dot{V} = 29.4$ mL/min, respectively.

Table II shows that the steric inversion diameters obtained for metal particles are much lower than those for polystyrene latex. This shift downward can be largely attributed to the

Table II. Experimental Conditions, Calibration Constants, and Predicted Steric Inversion Diameters for Various Calibration Plots Developed for Channel II^a

case/sample	rpm	\dot{V} (mL/min)	$G\Delta\rho \times 10^{-4}$ (g/s ² cm ²)	S_d	t_{r1} (min)	cc^b	d_i^c (μm)
A. PS	800	6.0	0.530	0.768	7.27	0.999	0.95
B. PS	1100	6.0	1.002	0.729	7.43	1.000	0.82
C. PS	1500	6.0	1.863	0.729	8.13	1.000	0.71
D. PS	1800	8.3	2.683	0.781	8.11	0.999	0.69
E. PS	1940	15.0	3.116	0.802	4.27	0.998	0.65
F. PS	2300	29.4	4.380	1.062	1.51	0.996	0.60
G. Cu ^d	421	29.4	23.19	0.686	1.94	0.991	0.39
H. Au ^e	1120	24.0	378.0	0.795	4.19	0.995	0.21

^a The calibrants used are polystyrene (PS) latex standards, copper particles, and gold particles with respective densities of 1.05, 8.9, and 19.2 g/cm³. ^b Correlation coefficient of the regression. ^c Calculated based on eq 11. ^d Sample g for Table I. ^e Sample a from Table I.

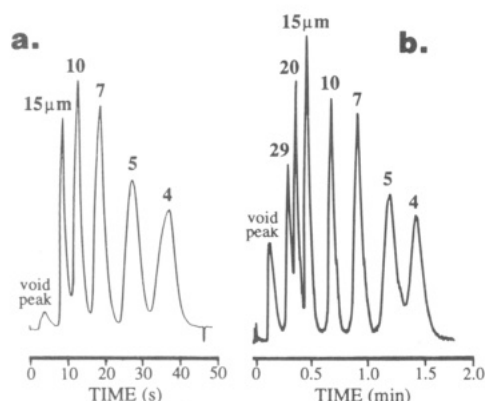


Figure 4. High-speed separation of polystyrene latex particles by sedimentation/steric FFF in channel II. The conditions for run a were 2300 rpm and \dot{V} = 29.4 mL/min and for run b 1940 rpm and \dot{V} = 15.0 mL/min.

increased $G\Delta\rho$ of the metal particles in agreement with eq 11. The reduced d_i values for metal particles confirms that the size analysis of metallic or other high-density particulate materials can be extended well into the submicrometer size range by sedimentation/steric FFF.

The enhanced risk of particle-wall adhesion at high $G\Delta\rho$ values discussed earlier was examined experimentally using gold sample a (Table I) spun at 1120 rpm in channel II. Various runs were made using stop-flow injection followed by elution flowrates ranging from 10 to 24 mL/min. When the channel was disassembled and visually examined after several such runs, a considerable deposit of gold particles was observed at the accumulation wall near the inlet. When the injection mode was switched to slow flow (5.0 mL/min) sample introduction followed by a run flow rate of 24 mL/min, the disassembled channel showed only traces of deposited metal particles after repeated runs had been made. It is possible that the injection flow rate could be further optimized but this was not done in this study.

Figure 5 shows the fractogram used to determine the calibration constants for case H in Table II. The fractogram was obtained for gold sample a in Table I. Fractions were collected from the eluting stream at frequent intervals for examination by electron microscopy. Figure 5 shows the electron micrographs obtained for fractions 3, 6, 13, and 21. The particle size within each fraction is seen to be quite uniform, confirming that the high resolution found for latex standards (Figure 4) is realized for metal particles as well. The diameter decreases with increasing retention time as is expected for steric mode operation (see Figure 1). The run conditions were 1120 rpm with a channel flow rate \dot{V} of 24.0 mL/min; the flow rate during slow flow injection was 5.0 mL/min. The latter flow rate was applied for 15 s, a time sufficient to cause the full relaxation of gold particles down to 0.1 μm at 1120 rpm. The breadth h_0 of the band deposited during

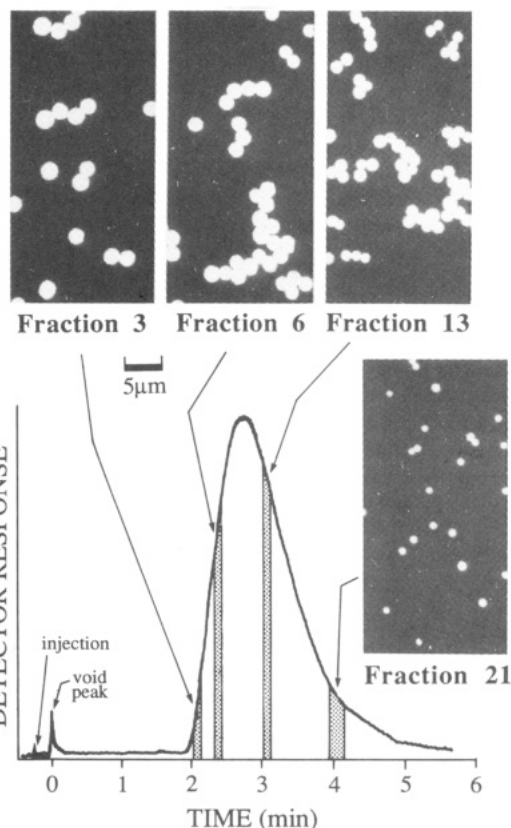


Figure 5. Fractogram and electron micrographs of fractions collected following the injection of gold sample a (Table I) into channel II. The spin rate was 1120 rpm, and the channel flow rate \dot{V} was 24.0 mL/min.

relaxation for a 1-μm gold particle under these conditions is only 0.4 cm, a distance contributing only negligibly to band broadening.¹⁷

Particle diameters were measured from the micrographs of 11 of the fractions collected from the run shown in Figure 5. The number of particles measured for each fraction ranged from 40 to 80. The results are shown in Table III. The data of Table III were used to construct the steric calibration plot shown in Figure 6. The diameter-based selectivity, equal to the negative slope of the linear regression line shown in Figure 6, was found to be 0.795. Using this and the other constants shown for calibration data set H in Table II, the inversion diameter was calculated to be 0.21 μm. The calibration constants obtained from this run were used for the subsequent particle size analysis of most of the metal samples including those consisting of gold particles and, by density compensation, other metal particles as well.

The conversion of the fractogram of gold particles shown in Figure 5 to particle size distribution curves is accomplished using eq 14 in conjunction with the calibration constants determined from the calibration plot of Figure 6. The

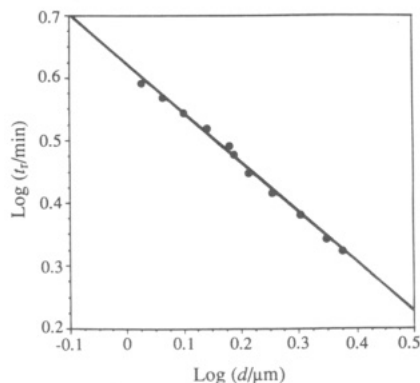


Figure 6. Steric calibration plot for gold particles obtained from the fractogram of Figure 5 and the microscopically measured particle diameters of fractions as reported in Table III.

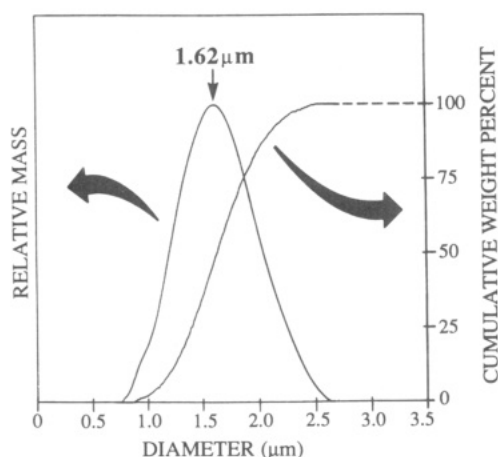


Figure 7. Particle size distribution curve for gold sample a (Table I) based on the fractogram of Figure 5 and the calibration plot of Figure 6.

Table III. Particle Diameters of the Fractions of Gold Sample a (from Table I) Collected during the Run Shown in Figure 5 and Used To Construct the Calibration Plot of Figure 6

fraction no. <i>N</i>	time (min)	particle diameter (μm)
3	2.05–2.15	2.37 ± 0.11
4	2.15–2.25	2.23 ± 0.13
6	2.35–2.45	2.01 ± 0.13
8	2.55–2.65	1.80 ± 0.13
10	2.75–2.85	1.64 ± 0.14
12	2.95–3.05	1.55 ± 0.17
13	3.05–3.15	1.51 ± 0.14
15	3.25–3.35	1.39 ± 0.16
17	3.45–3.55	1.26 ± 0.13
19	3.65–3.75	1.16 ± 0.08
21	3.95–4.15	1.06 ± 0.12

conversion was carried out using our in-house software. The resulting particle size distribution curves for gold sample a are shown in Figure 7. These and subsequent size distribution curves have been corrected for light scattering such that the ordinate scale represents relative mass. Thus the particle size distribution curves give a mass-based distribution.

Cumulative mass distribution parameters obtained from the cumulative size distribution curve shown in Figure 7 for gold sample a are shown in Table I (along with other FFF-derived values). The values reported show significant departures from the size parameters (also reported in Table I) based on light scattering. Thus the 50% cumulative mass distribution diameter obtained by sedimentation/steric FFF is 1.63 μm (the mode diameter is 1.62 μm) compared to 2.60 μm for the 50% point obtained by light scattering. The 90% cumulative point obtained by light scattering was 5.02 μm

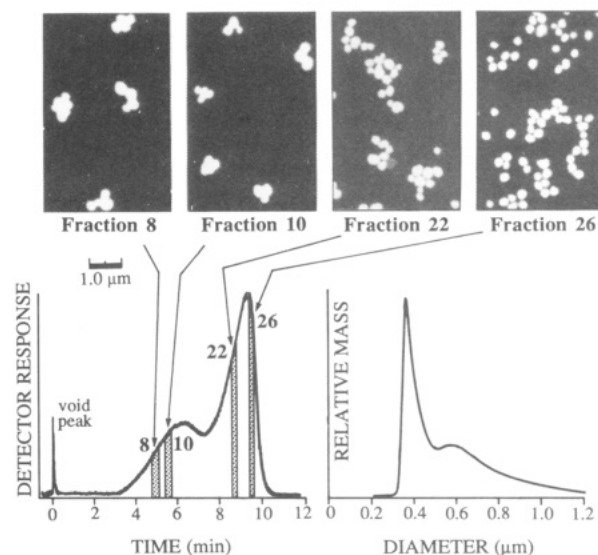


Figure 8. Fractogram and particle size distribution of gold sample b obtained under same experimental conditions as reported in Figure 5. The electron micrographs show that the first peak in the fractogram (the second peak in the bimodal size distribution) is composed of particle aggregates.

compared to 2.15 μm obtained in our FFF experiments. (The maximum diameter suggested by FFF was 2.7 μm.) It is noteworthy that the validity of our results is supported by microscopy, not only in terms of the direct measurement of the diameters of fractions but also from the fact that few particles as large as 3 μm and no particles larger than 3.5 μm were observed in any of the fractions or in the original material. (Somewhat better agreement between the two methods was found for other metal samples as confirmed in Table I.)

The fractionation of the second sample of gold particles, gold sample b, and the electron microscopy of fractions has provided a wealth of detail on the existence and distribution of particle aggregates in this sample. The fractogram for this material, obtained under the same experimental conditions as reported for Figure 5, is shown in Figure 8 along with a few characteristic micrographs. The micrographs show that the larger particles consist mainly of aggregates of the smaller particles. Thus the first peak of the bimodal distribution consists largely of aggregated particles. The aggregates in fraction 8 appear to consist primarily of quadruplets and quintuplets of elementary particles while those collected in fraction 10 are mainly triplets and quadruplets. As one passes along to fraction 22, which is eluted with the second peak of the fractogram, individual particles begin to appear in association with a few remaining doublets. Fraction 26 displays a population consisting mainly of single particles with diameters around 0.3 μm.

When the fractogram shown in Figure 8 is converted into a particle size distribution curve using the calibration plot and associated parameters of Figure 6, the size distribution curve shown on the rhs of Figure 8 is obtained. This curve is subject to two distortions. First, as discussed in the Theory section in connection with eq 14, it does not accurately size some of the smaller particles between 0.2- and 0.3-μm diameter that elute in the steric transition range. (This distortion could be largely corrected by using eq 15.) Second, the size reported for the irregular aggregate particles will be larger than the equivalent spherical diameter, probably in closer accord to (or slightly larger than) the maximum particle length. These distortions are offset by the fact that the nature of each fraction can be defined to any desired detail by microscopic observation and analysis. The few microscopic observations provided here make it clear that the first peak of the bimodal

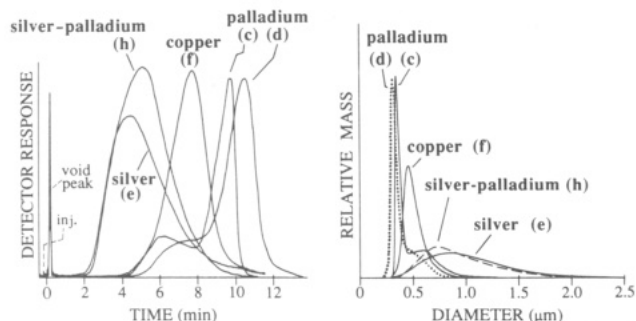


Figure 9. Fractograms and size distribution curves for five metal samples. By using the same flow rate (24.0 mL/min) and adjusting field strength according to the density compensation procedure ($G\Delta\rho = \text{constant}$), the calibration plot obtained for gold (shown in Figure 6) was applicable and could be used to obtain all size distribution curves.

size distribution (the second peak of the fractogram) is due to single particles mixed with a few low-order aggregates and that the second peak is due to larger clusters of elementary particles. This information would be difficult to acquire by other methods which cannot be combined with microscopy. In addition, most other methods do not have the high-resolution characteristic of sedimentation/steric FFF. Furthermore, a size analysis obtained by electron microscopy alone would be difficult to obtain because of the complex and varied geometry of the aggregates and the difficulty of distinguishing isolated particles that make direct contact with one another during microscopy.

Figure 9 shows the fractograms for five additional metal samples containing particulate palladium (c and d), silver (e), copper (f), and silver-palladium (h); the letter designations in parentheses after each metal are those assigned to the corresponding metals in Table I. For each sample the $G\Delta\rho$ value and the flow rate were kept at the same level as that used for gold in Figure 5, thus allowing use of the calibration plot shown in Figure 6. Because of density variations among the metals, this required adjustment of the rotation rate when running different metallic samples. Thus while gold samples a and b (Table I) for which density $\rho = 19.2 \text{ g/cm}^3$ were run at 1120 rpm, the spin rate was changed to 1465 rpm for palladium samples c and d ($\rho = 11.6 \text{ g/cm}^3$), 1550 rpm for silver sample e ($\rho = 10.5 \text{ g/cm}^3$), 1700 rpm for copper sample f ($\rho = 8.9 \text{ g/cm}^3$), and 1474 rpm for silver-palladium sample g ($\rho = 11.5 \text{ g/cm}^3$). The resulting size distribution curves for these metals are also shown in Figure 9.

Of the fractograms displayed in Figure 9, only those for palladium samples c and d show a tendency toward bimodality as was characteristic of the fractogram for gold sample b displayed in Figure 8. This type of fractogram and the resulting size distribution curves suggest the presence of a significant population of aggregated particles. However, confirmation of aggregation by the electron microscopy of collected fractions was not carried out in these cases.

For copper sample g, new run conditions were established to increase the speed of analysis. (A significant increase in speed will result simply from the larger minimum particle size of this sample.) Thus the flow rate (still using channel II) was increased from 24.0 to 29.4 mL/min and the rotation rate reduced from 1700 to 421 rpm. Figure 10 shows that the run was completed in 1 min following slow flow injection. Again, the collected fractions show the expected size discrimination, proceeding from large to small particles with increasing time.

Since the $G\Delta\rho$ and V conditions were changed relative to those used for the other metal samples, a new calibration plot was required. Once again this was obtained by measuring the mean diameter of particles collected in different fractions and making the usual logarithmic plot (see Figure 6) of

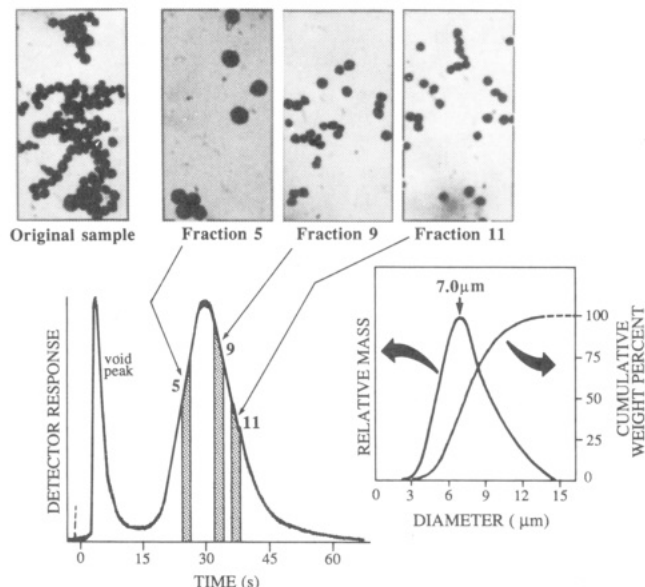


Figure 10. Fractogram and size distribution curves of copper sample g along with optical micrographs of collected fractions from run in channel II at 421 rpm and 29.4 mL/min.

retention (collection) time versus the microscopically measured diameter. The parameters S_d and t_{r1} were found to be 0.686 and 1.94 min, respectively. The resulting size distribution curves for this metal are shown on the rhs of Figure 10. (Parts of Figure 10 were shown in a recent review article, but two of the micrographs and the cumulative distribution curve are new.⁶)

CONCLUSIONS

The experimental results presented above confirm that particle size analysis by sedimentation/steric FFF, normally applied to particle above 1- μm diameter, can be extended significantly into the submicrometer size range, at least down to diameters of 0.2–0.3 μm . The high-resolution characteristic of large particle fractionation and size characterization by Sd/St FFF is found to persist into the smaller size range as confirmed by electron microscopy. The normally sluggish elution of smaller particles in the steric mode is largely offset by using a channel of reduced thickness and volume and by using high flow rates.

For practical particle size analysis, the modified Sd/St FFF procedure developed here is thus characterized by high resolution and accuracy as well as by high speed and a capability for extending deeply into the submicrometer size range. The technique has the additional advantage over other particle sizing methods of providing narrow fractions for further characterization by microscopy and other procedures. A linkage with microscopy is particularly useful when aggregates or other unusual particle structures contribute to the size distribution.

The calibration procedure using density compensation (i.e., a constant value of $G\Delta\rho$) has been found particularly useful here where maximum G values are not sufficiently high to obtain a calibration plot from latex standards, a procedure requiring only a few minutes. In the present case it was necessary to establish calibration constants using a series of average particle diameters measured from the micrographs of collected fractions. This procedure, while not difficult, is certainly more laborious than latex calibration, and it is thus useful to have a means (via density compensation) to apply a single calibration plot to a large group of particulate materials whose densities may vary significantly from case to case.

The principle of extending sterically based size analysis well into the submicrometer size range using high $G\delta\rho$ values could obviously be extended to lower density materials by using higher field strengths. Unfortunately, suitable instrumentation is not readily available for this purpose. Much of the existing high spin rate instrumentation cannot be readily utilized with the high flow rates or thin channels required here. In addition, most high spin rate FFF instruments have a vertical axis of rotation, which means that larger particles will be driven toward the channel edges by gravity during the FFF run. Displacement into the edge regions leads to abnormal particle migration and possibly particle deposition. While this effect may not be significant for submicrometer sized particles near the steric inversion diameter, it can become serious for particles at the high end of the size distribution curve.

An alternative to the use of high G values to extend the steric mode analysis of low density particles into the submicrometer size range is to use flow FFF instead of sedimentation FFF. The cross-flow driving force used in flow FFF can be more readily adjusted to extreme values than can the corresponding driving forces of sedimentation FFF.¹⁴ Thus the inversion diameter d_i in flow FFF has already been driven as low as 0.3 μm , a result applicable to all particles without regard to their density. Work is continuing to reduce the inversion diameter in flow FFF even more to further broaden the applicable size range.

The use of high flow rates in thin channels of reduced breadth and cross sections as reported in this study has pushed certain flow and hydrodynamic parameters to levels that are unusually high for FFF. Thus when channel II is operated at the maximum flow rate reported here, 29.4 mL/min, the linear flow velocity $\langle v \rangle$ is almost 40 cm/s. In addition, the Reynolds number approaches 50, and the shear rate at the wall acquires a level of about 18 000 s^{-1} . These are 2 orders of magnitude greater than values realized in typical normal mode FFF operation.

ACKNOWLEDGMENT

This work was produced under Grant CHE-9102321 from the National Science Foundation. The authors are grateful to Dan Goia of Metz Metallurgical Corp. for supplying the metal samples.

GLOSSARY

b	channel breadth
c	sample concentration
C'	constant
d	particle diameter
d_i	steric inversion diameter
G	acceleration
kT	thermal energy
K	constant defined by eq 18
L_{tt}	tip-to-tip channel length
$m(d)$	particle size distribution
R	retention ratio
r_a	ratio of actual to sterically predicted dt_r/dd
r_t	ratio of actual to sterically predicted t_r
S_d	diameter based selectivity
t_r	retention time
t_{r1}	extrapolated steric retention time for 1- μm particles
t^0	void time
$\langle v \rangle$	mean flow velocity
\dot{V}	volumetric flow rate
w	channel thickness
α	constant
β	constant
γ	steric correction factor
Δ	dimensionless particle diameter, d/d_i
$\Delta\rho$	particle-carrier density difference

RECEIVED for review June 9, 1992. Accepted September 1, 1992.

Registry No. Au, 7440-57-5; Pd, 7440-05-3; Ag, 7440-22-4; Cu, 7440-50-8.